Supplementary Information

Molecular Principles of Redox-Coupled Protonation Dynamics in Photosystem II

Friederike Allgöwer[1], Ana P. Gamiz-Hernandez[1], A. William Rutherford[2], Ville R. I. Kaila[1,*]

[1] Department of Biochemistry and Biophysics, The Arrhenius Laboratories for Natural Sciences, Stockholm University, SE-106 91, Stockholm, Sweden.
[2] Department of Life Sciences, Imperial College London, London SW7 2AZ, United Kingdom.

* Corresponding author: Ville R. I. Kaila

Email: ville.kaila@dbb.su.se

This PDF file includes:

Elaboration on Models, Methods, and Mechanisms
Figures S1 to S9
Tables S1 to S6
Movies S1 to S3

Elaboration on models, methods, and mechanisms

Elaboration of steps involved in the $S_2Y_z \rightarrow S_3Y_z$ transition

General elaboration on the models: The $S_2Y_z \rightarrow S_3Y_z$ transition was modeled by considering both the closed cubane form in the high spin state (Figure S2A, top panel) and the open cubane form in the low spin state (Figure S2A, bottom panel), as suggested by previous findings.[1-7] The $S_2Y_z \rightarrow S_3Y_z$ step is initiated from S_2Y_z (not shown in the figure) by oxidation of the Tyr_z to $Tyr_z^{\bullet}$, which couples to a proton transfer from Tyr_z to His190 and formation of the $S_2Y_z^{\bullet}$ state (Figure S2A, panel *iii*). In both the HS (Figure S2A, *top*) and LS (Figure S2A, *bottom*) forms of $S_2Y_z^{\bullet}$, W3 establishes a hydrogen-bonded array via a nearby water (W_{c9}) to W2, and further via two water molecules (W_{c109}, W_{c121}) to Asp61 (Figure S2A, panel *i* and *iv*).

In the **HS/close cubane form**, the W3 deprotonates via W_{c9} to W2 (Figure S2A, panel *i)*, which couples to the migration of W3 to Mn4 (Figure S2A, panel *ii*). This step leads to the further proton transfer via the two intervening water molecules to Asp61 (Figure S2A, panel *iii*), and the further formation of S_3Y_z by re-reduction and protonation of Tyr_z by His190 (Figure S2A, top *right* panel, S_3Y_z). The energy diagram of this transition is shown in panel Figure S2B, and the optimized reaction pathway in Movie S1. The two HS energy profiles are shown in Figure S2D, as well as in main text Figure 2A.

In the **LS/open cubane form**, the W3 also deprotonates via W_{c9} to W2 (Figure S2A, panel *iv*), which couples to the migration of W3 to Mn1 (Figure S2A, panel *v*). This step leads to the further proton transfer via the two intervening water molecules to Asp61 (Figure S2A, panel *vi*), and the further formation of S_3Y_z by re-reduction and protonation of Tyr_z by His190 (Figure S2A, bottom *right* panel, S_3Y_z). The energy diagram of this transition is shown in panel Figure S2C (with W3 restricted to Ca^{2+}), Figure S2E (no W3 restrictions), and the optimized reaction pathway is shown in Movie S2.

Effect of W3 migration: We find that the energetics of the W3-mediated proton transfer to Asp61 is affected by the migration of W3 to Mn4/Mn1: the barrier for the initial proton transfer from W3 to W2 increased by 8 kcal mol^{-1} when the position of W3 was restrained to remain on the Ca^{2+} during the reaction (Figure S2B for HS/closed, Figure S2C for LS/open). The migration of the W3 leads to a small conformational change of surrounding residues, particularly Arg357 and Ala344 (Figure S2G), which has been shown to be crucial for the Mn_4O_5Ca cluster.[8]

Effect of Tyr oxidation on the proton transfer reaction: To probe the effect on the Tyr oxidation on the proton transfer from W3 to Asp61, we removed the His190/Tyr_z pair from the DFT cluster models, and re-computed the energy profile. The removal of the Tyr/His has almost no effect on the energy profile in the S_2Y_z state, whereas the proton transfer barrier is increased by around 6 kcal mol^{-1} in the $S_2Y_z^{\bullet}$ state (Figure S2F), suggesting that the reaction is sensitive to the electrostatic effect from $Tyr_z/HisH^+$. Previous studies also support that the Tyr_z oxidation has an electrostatic influence on the Mn_4O_5Ca cluster.[9]

Elaboration of QM/MM MD modelling of the $S_2Y_z \rightarrow S_3Y_z$ transition

QM/MM MD simulations were performed as described in the main text methods section to probe the effect of protein dynamics and explicit surroundings on the $S_2Y_z \rightarrow S_3Y_z$ transition. Due to limited (8-10 ps) QM/MM MD sampling timescale, we do not observe a spontaneous complete proton transfer from W3 to Asp61. However, in all QM/MM MD simulations of the $S_2Y_z^{\bullet}$ state, we observe a hydrogen-bonded water wire that is strongly oriented from W3 towards Asp61 (Figure S3A, B).

In the low spin open cubane form of the $S_2Y_z^{\bullet}$ state, we observe a transient protonation of Asp61 by W1 (Figure S3C), resembling previous observation from QM/MM MD calculations performed at the PBE+U/MM level.[10-11] In another QM/MM trajectory of the same low

spin open cubane form of the $S_2Y_z^{\bullet}$, we observe proton transfer between W1 and W3 (Figure S3E). These findings support the effective protonic connectivity between W3 and Asp61.

The high spin closed cubane form of the $S_2Y_z^{\bullet}$ state, show that the deprotonated W3 spontaneously migrates to Mn4 (Figure S3B), similar to what we observe in the DFT cluster models. This W3 migration leads to a shift of W4 into the vacant W3 position (Figure S3F), while a nearby water molecule binds to Ca^{2+}, from the so-called "water wheel"-region,[12] replacing the initial W4 position.

The QM/MM MD simulations of the S_3Y_z state in both HS and LS forms, support that the water/hydroxy ligands connected to Mn4 can rotate during the simulation, and exchange their character (W3→W2, W2→W1).

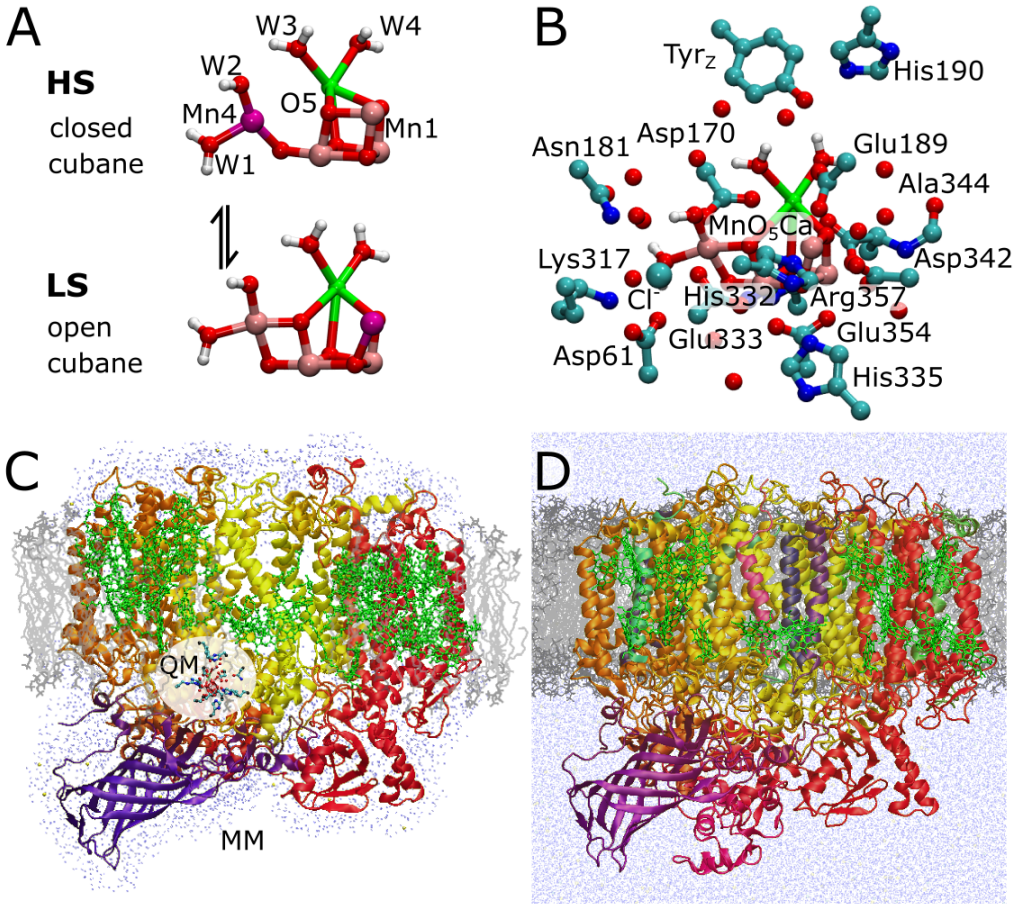

Figure S1. Multi-scale molecular simulation models of PSII. (A) Open (LS, *S*=1/2) and closed (HS, *S*=5/2) conformations of the S_2Y_z state. Mn^{III} in purple, Mn^{IV} in pink. See Figure S2 for energetics. (B) DFT model used for modeling the $S_2Y_z \rightarrow S_3Y_z$ and $S_3Y_z \rightarrow S_4Y_z$ transitions. (C) QM/MM MD model of PSII, showing the active site (QM region) and the surrounding protein system (MM region) (see *Methods*). (D) Atomistic molecular dynamics (MD) model of PSII.

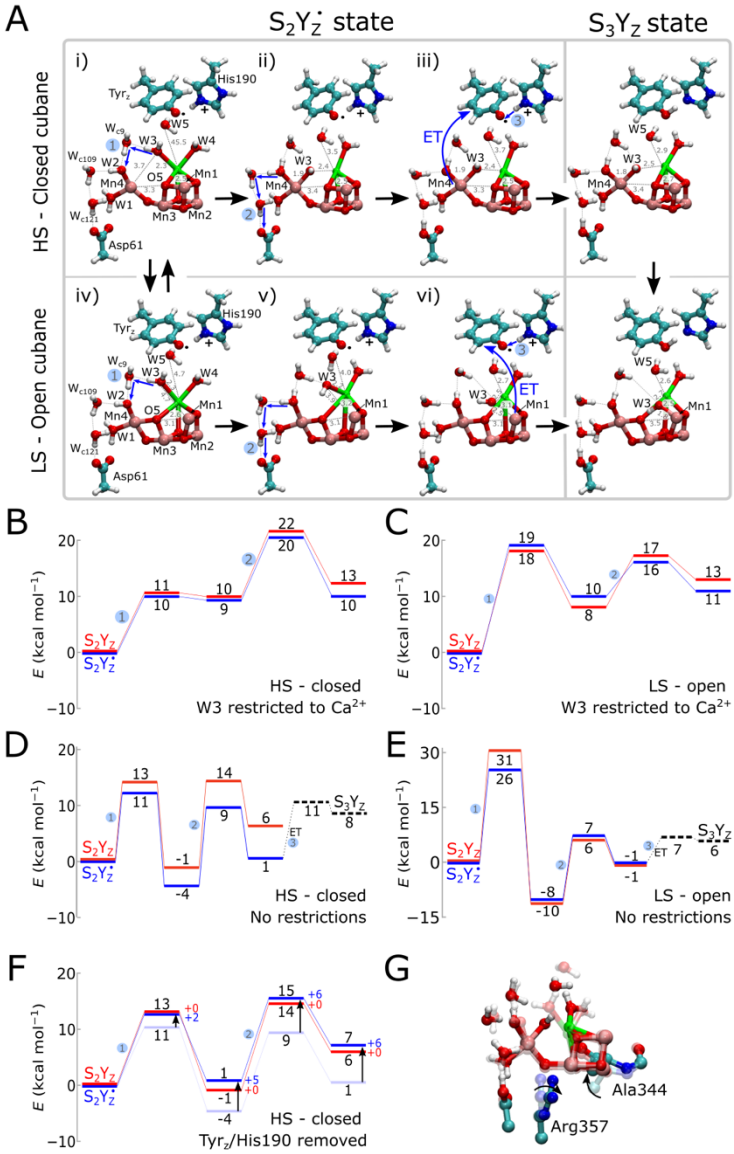

Figure S2. Structure and energetics of redox-driven proton transfer from W3 to Asp61 in the $S_2Y_z \rightarrow S_3Y_z$ transition. (A) Molecular structures of intermediate states along the proton transfer reaction from W3 to Asp61 in HS/closed cubane and LS/open cubane structures of the $S_2Y_z^{\bullet}$ and S_3Y_z states. See more detailed description of steps i-vi in SI Elaboration of models, methods, and mechanisms. (B), (C) Energetics of the proton transfer from W3 to Asp61 in (B) HS form and (C) LS form of S_2Y_z and $S_2Y_z^{\bullet}$ with W3 restricted to bind to Ca^{2+}. (D), (E) Energetics of proton transfer from W3 to Asp61 in the (D) HS and (E) LS form of S_2Y_z and $S_2Y_z^{\bullet}$, allowing for the migration of W3 to Mn4/Mn1 (see main text Figure 2 for combined HS/LS energy diagram). (F) Removal of the His190/Tyr_z pair increases the proton transfer barrier by around 6 kcal mol^{-1} in the $S_2Y_z^{\bullet}$ state (in blue), whereas the barrier remains nearly unaffected in the S_2Y_z state ($\Delta E^{\ddagger} \sim 0$ kcal mol^{-1}). (G) Migration of W3 couples to a subtle conformational change in Arg357 and Ala344.

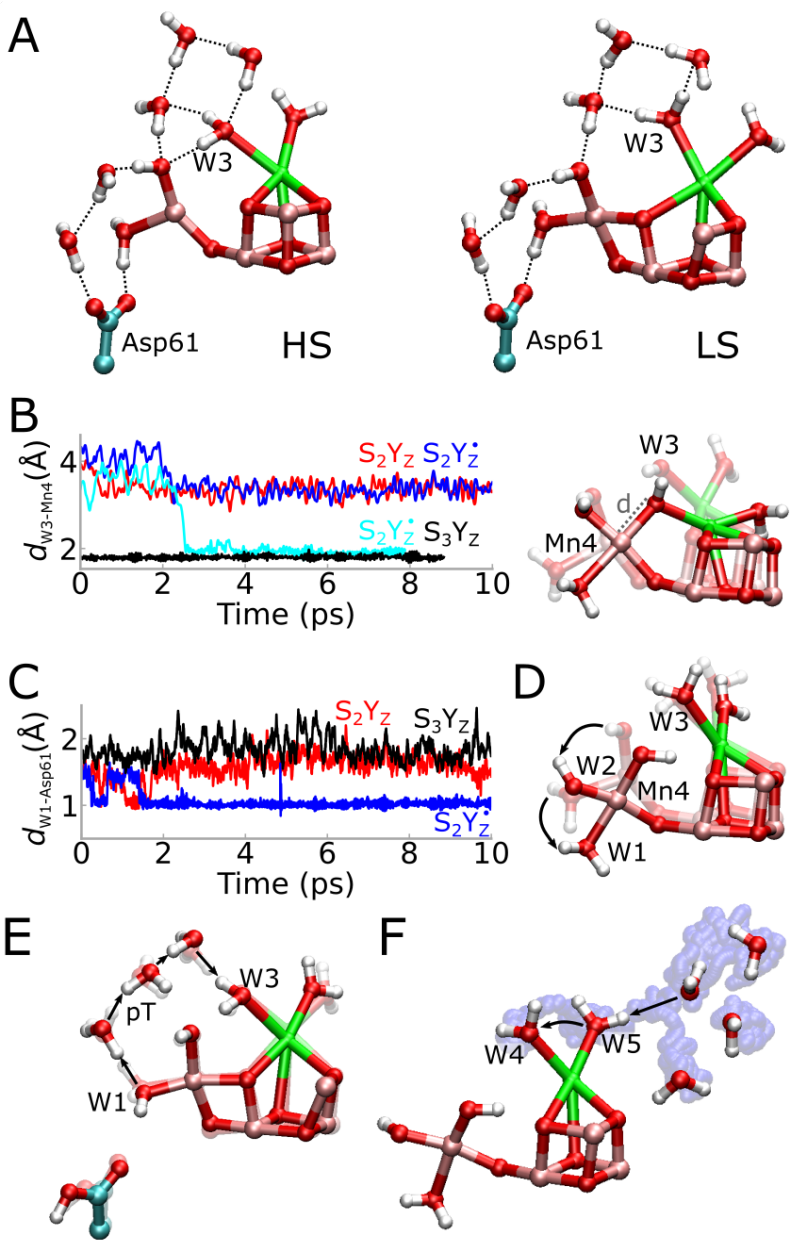

Figure S3. QM/MM MD simulations of the $S_2Y_z \rightarrow S_3Y_z$ transition. (A) Snapshots of molecular structures from QM/MM MD simulations showing the hydrogen bonding network between W3 and Asp61. (B) In the $S_2Y_z^\bullet$ state (HS/closed: Asp61 protonated, W3 deprotonated/Asp61 deprotonated, W3 protonated in light blue/dark blue, respectively), the deprotonated W3 spontaneously migrates during the initial 3 ps of the simulation and coordinates to Mn4, supporting the re-organization of the ligand water structure. (C) Transient protonation of Asp61 by W1 in the $S_2Y_z^\bullet$ state. (D) In the S_3Y_z state, the W1-W3 water/hydroxo ligands connected to Mn4 rotate during the simulation in both HS and LS states. (E) In the $S_2Y_z^\bullet$ state (LS/open: Asp61 protonated, W3 deprotonated) a spontaneous proton transfer between W1 and W3 is observed, supporting the proposed proton transfer pathway with W3 as the proton donor. F) Upon migration of W3 to Mn4 in the S_3Y_z HS state, W4 shifts into the vacant W3 position, while a nearby water molecule binds to Ca^{2+}, replacing the initial W4 position. This water molecule originates from a water cluster (time average shown in transparent blue) of the O1 channel proposed in Ref. 13 (main text references).

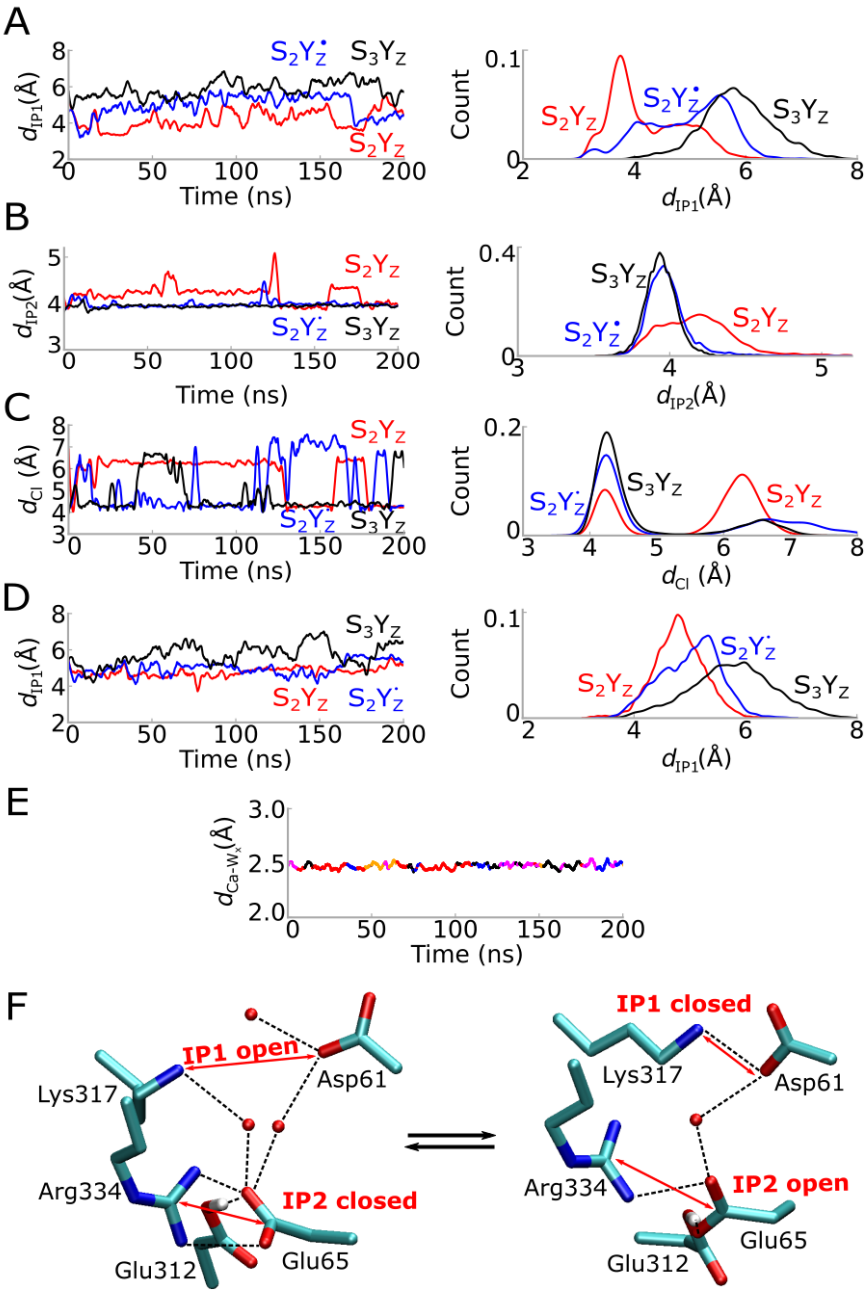

Figure S4. Atomistic MD simulations of PSII. Distance between headgroups and distance distributions of (A) the Asp61/Lys317 ion-pair (d_{IP1}) at T=320 K, (B) the Glu65/Arg334 ion-pair (d_{IP2}) at T=320 K, (C) Cl^- and Arg334 at T=320 K (d_{Cl}, see also main text Figure 2C), and (D) the Asp61-Lys317 ion-pair (d_{IP1}) at T=300 K, showing similar trends as the simulations performed at T=320 K. IP1 and IP2 are anti-correlated, whereas closing of IP1 and opening of IP2, lead to a *ca*. 2 Å increase of the d_{Cl} distance. (E) In MD simulations performed after the migration of the W3 to Mn1 (S_3Y_Z state), the vacant W3 position is filled by surrounding water molecules (called W5 in our DFT calculations). The figure shows the distances ($d_{Ca\text{-}Wx}$) between the Ca^{2+} and this exchanging water ligands (indicated in different colors). (F) Open and closed conformations of the Lys317-Asp61 ion-pair (IP1) and Glu65-Arg334 (IP2). Hydrogen bonds are shown as dashed lines.

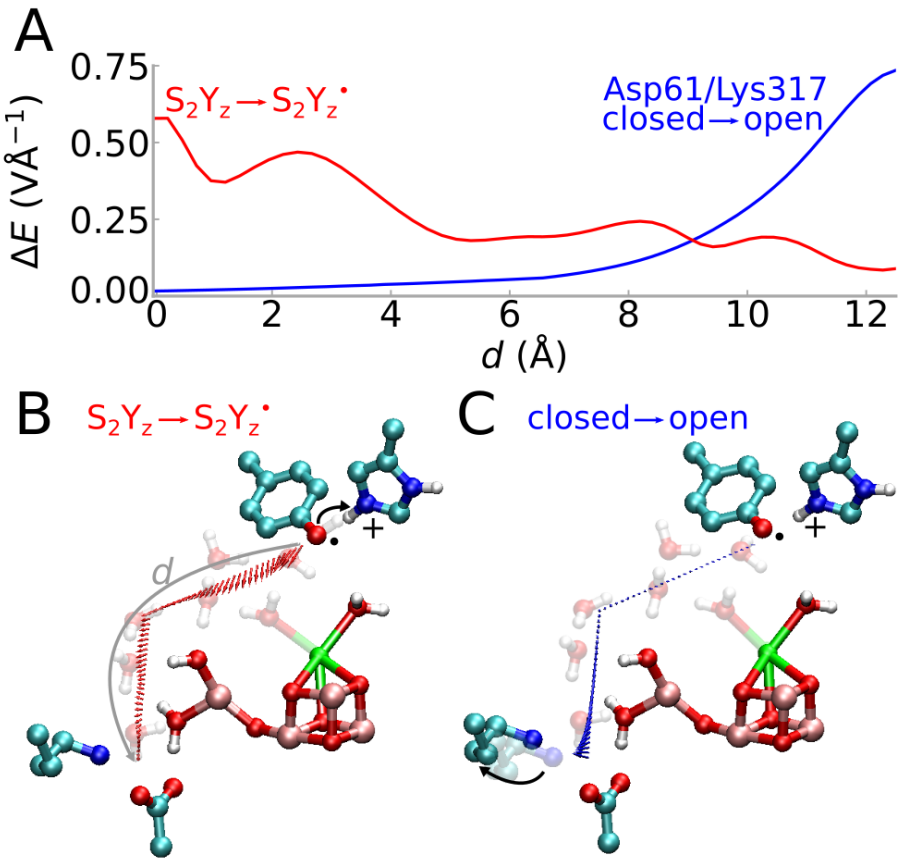

Figure S5. Redox-driven electric field formation between His190 ($HisH^+$) and Asp61. (A) Formation of the Tyr_z radical/cationic His190 ($HisH^+$) in the $S_2Y_z \rightarrow S_2Y_z^{\bullet}$ transition and opening of the Asp61/Lys317 ion-pair result in an increase in the electric field along the proton pathway (*d*). While the protonation of His190 mainly affects the electric field of the first part of the reaction (*d*=0-8 Å), opening of the Asp61-Lys317 ion-pair, which is favored by the formation of $S_2Y_z^{\bullet}$, increases the electric field vector along the last part of the proton pathway (*d*=8-12 Å). (B) Differences in electric field vectors due to (B) the $S_2Y_z \rightarrow S_2Y_z^{\bullet}$ transition, and (C) the Asp61/Lys317 ion-pair opening.

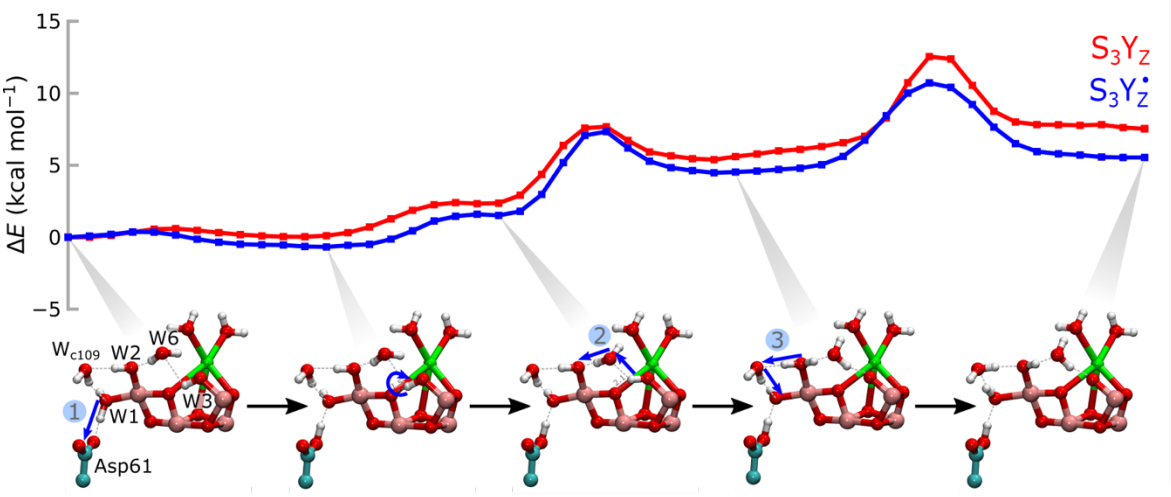

Figure S6. Energetics and structures of intermediate states of the proton transfer in the $S_3Y_Z \rightarrow S_4Y_Z$ transition. The figure shows intermediate states along the W3(OH^-)-W6 -W2-Wc109-W1-Asp61 pathway. Energies at B3LYP*-D3/def2-TZVP/ε=4 level of theory are reported in (kcal mol^{-1}).

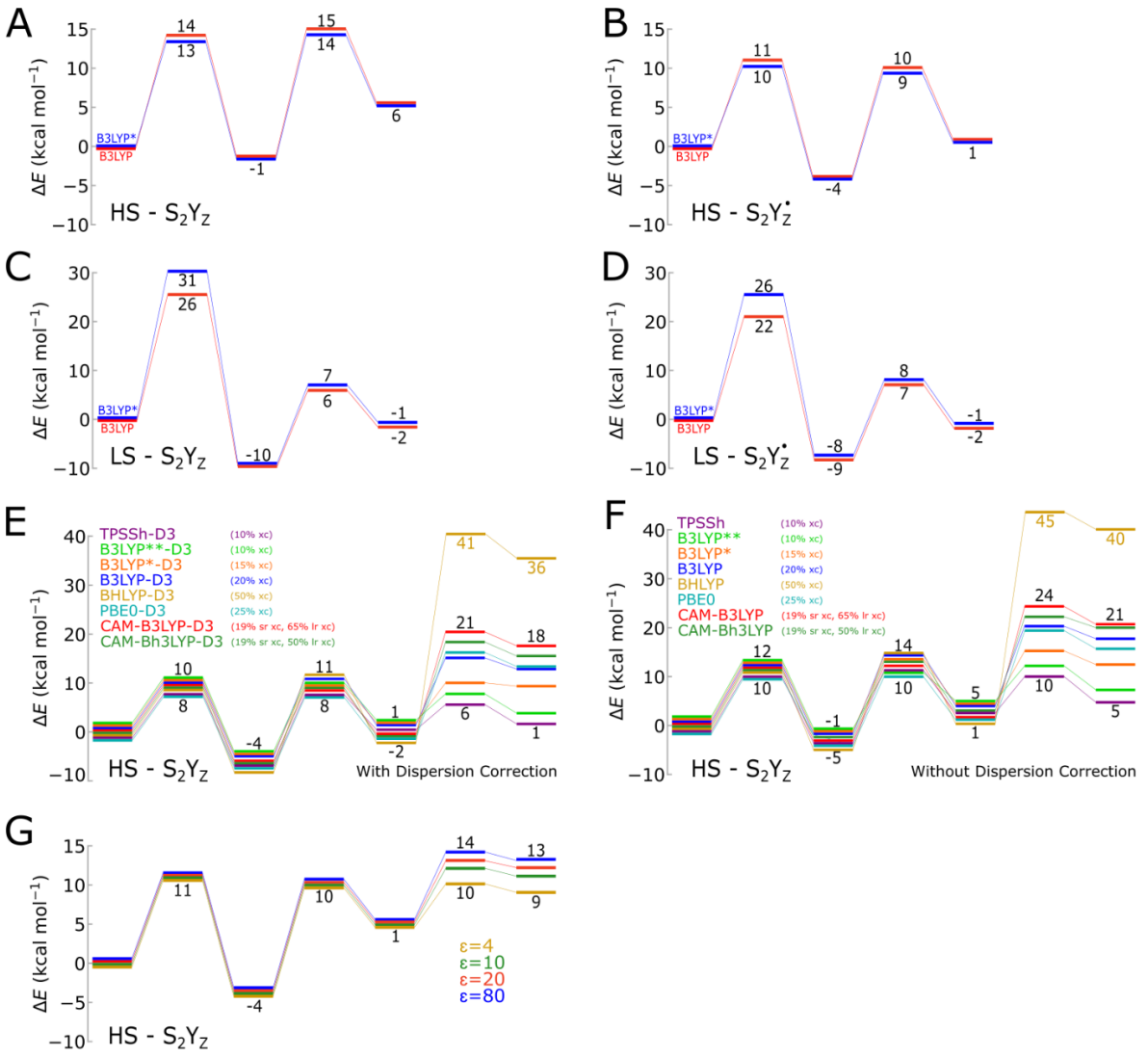

Figure S7. Benchmarking the energetics of proton transfer from W3 to Asp61 in the S_2Y_z and $S_2Y_z^{\bullet}$ states in the (A), (B) HS and (C), (D) LS states. Geometry optimizations were performed at the B3LYP-D3/def2-SVP/def2-TZVP(Mn,Ca,Cl)/ε=4[13-16] level of theory, and single point energies were calculated at the B3LYP*-D3/def2-TZVP/ε=4[17] (blue line) or B3LYP-D3/def2-TZVP/ε=4 (red line) levels of theory. (E), (F) Benchmarking the energetics of the $S_2Y_z^{\bullet} \rightarrow S_3Y_z$ transition with different density functionals, with varying amount of exact exchange (xc), with (E) or without (F) including empirical dispersion correction. The calculations were performed with TPSSh[18](10% xc, purple), B3LYP** (10% xc, light green), B3LYP* (15% xc, orange), B3LYP (20% xc, dark blue), BHLYP[19] (50% xc, yellow), CAM-B3LYP[20] (19% short-range xc, red; 65% long-range xc), CAMh-B3LYP[21] (19% short-range xc, dark green; 50% long-range xc), and PBE0[22] (25% xc, light blue). All calculations employed the def2-TZVP basis sets and ε=4. BHLYP was used to screen the effect exact exchange, although this functional is known to perform rather poorly on predicting the energetics. These calculations, nevertheless, support that the final step involving a Tyr_z oxidation, may have a charge transfer character. (G) Benchmarking the effect of the dielectric constant on the reaction energetics.

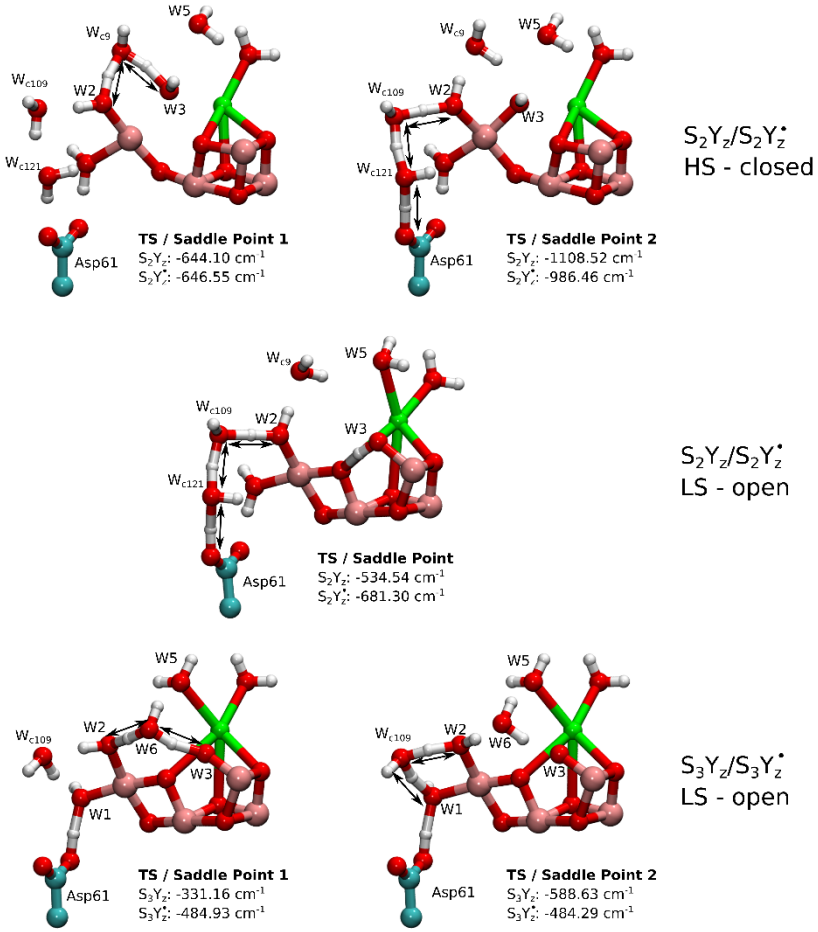

Figure. S8. Structure of key transition states (TS) / saddle points obtained from DFT reaction pathway optimizations, showing the vibrational displacement along the imaginary frequency normal mode.

Figure S9. Comparison of XFEL structures of S3 with the current DFT model of the S_3Y_z (LS) state. Structures/models: 3WU2,[23] 5WS6,[24] 6JLL, 6JLO[25], 6W1Q-6W1V,[26] 7RF4-7RF8,[27] and for the DFT models: Siegbahn2013,[28] Batista 2016,[29] Kaila 2016,[4] Yamaguchi 2016,[30] Pantazis 2021.[31]

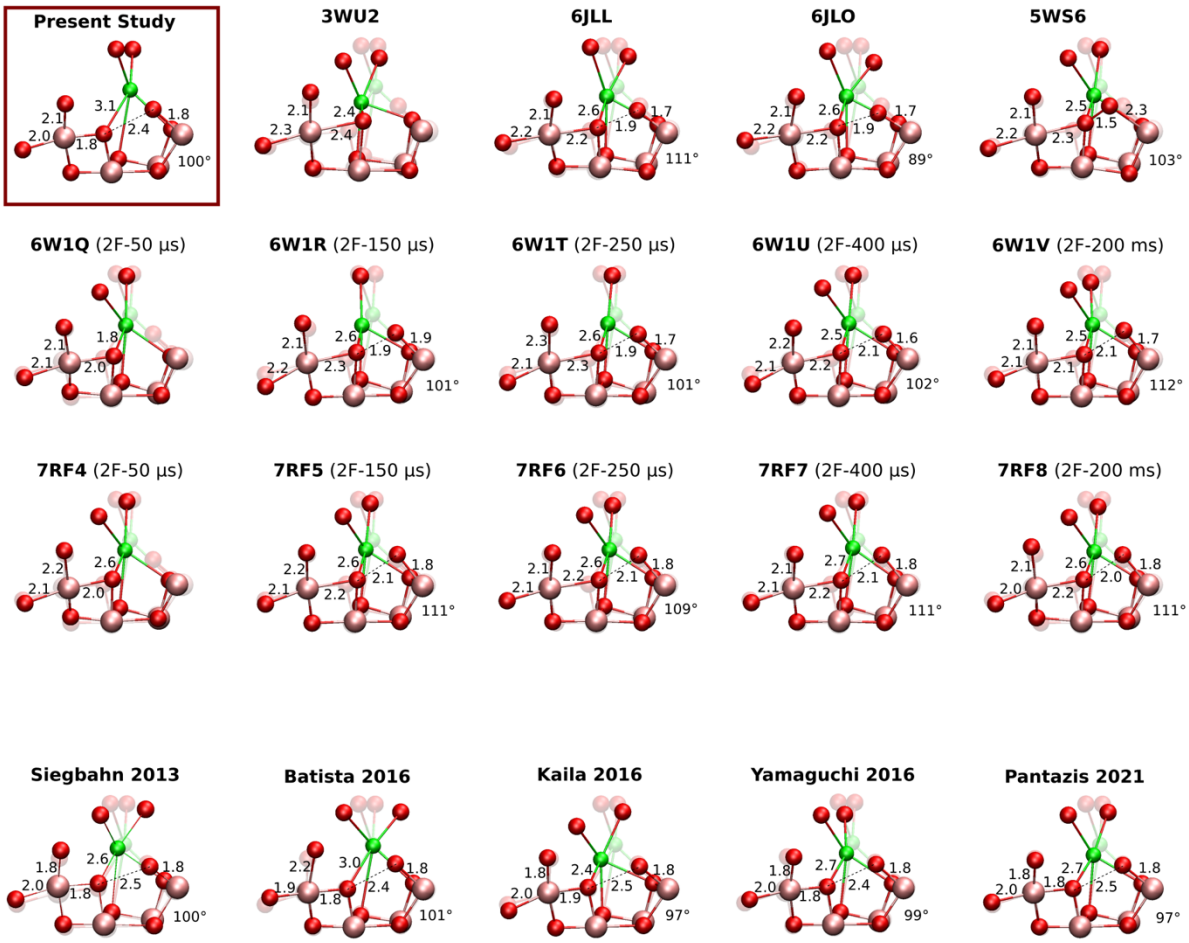

Table S1. List of residues included in the DFT models and details of the modeled states.

Mn_4O_5Ca cluster Ligand waters (W1-W4) $Asp61^{D1}$, $Tyr161^{D1}$, $His190^{D1}$, $Lys317^{D2}$, $Asn181^{D1}$, Cl^- 13 crystal waters (W_{c9}, W_{c11}, W_{c64}, W_{c67}, W_{c68}, W_{c72}, W_{c97}, W_{c109}, W_{c121}, W_{c123}, W_{c158}, W_{c512}, W_{c580}) $His332^{D1}$, $Asp342^{D1}$, $Ala344^{D1}$ (included backbone), $Leu343^{D1}$ (included C and O) $Glu333^{D1}$, $Asp170^{D1}$, $Glu189^{D1}$, $Glu354^{CP43}$, $His337^{D1}$ ($HisH^+$), $Arg357^{CP43}$	***N* = 212 atoms** (***N*=211** atoms in S_3Y_z with proton removed from Asp61) (***N*=210** atoms in S_4Y_z with proton removed from Asp61)

State	Q_{tot}	S_{tot}	Oxidation states
S_2Y_z	+1	HS	Mn1(IV), Mn2(IV), Mn3(IV), Mn4(III), Tyr_z
		LS	Mn1(III), Mn2(IV), Mn3(IV), Mn4(IV), Tyr_z
$S_2Y_z^{\bullet}$	+2	HS	Mn1(IV), Mn2(IV), Mn3(IV), Mn4(III), $Tyr_z^{\bullet}$
		LS	Mn1(III), Mn2(IV), Mn3(IV), Mn4(IV), $Tyr_z^{\bullet}$
S_3Y_z (Asp61 protonated)	+2	HS	Mn1(IV), Mn2(IV), Mn3(IV), Mn4(IV), Tyr_z
		LS	Mn1(IV), Mn2(IV), Mn3(IV), Mn4(IV), Tyr_z
S_3Y_z (Asp61 deprotonated)	+1	LS	Mn1(IV), Mn2(IV), Mn3(IV), Mn4(IV), Tyr_z
$S_3Y_z^{\bullet}$	+2	LS	Mn1(IV), Mn2(IV), Mn3(IV), Mn4(IV), $Tyr_z^{\bullet}$
S_4Y_z (Asp61 deprotonated)	+1	LS	Mn1(IV), Mn2(IV), Mn3(IV), Mn4(IV), Tyr_z, $W3{:}O^{2-\bullet}$
S_0Yz	+1	LS	Mn1(III), Mn2(IV), Mn3(III), Mn4(III), Tyr_z, O_2

Table S2. Relative electronic energies (B3LYP*-D3/def2-TZVP/ε=4) along the S_2Y_z/S_3Y_z transition (in kcal mol^{-1}).

	S_2Y_z	$S_2Y_z^{\bullet}$	S_3Y_z
HS/closed	0.3	1.4	14.8
LS/open	0	0	0

Table S3. List of performed QM/MM MD simulations.

Nr.	State	Spin	Length
1	S_2Y_z	HS	10 ps
2		LS	10 ps
3	$S_2Y_z^{\bullet}$	HS	10 ps
4		HS, W3 deprotonated, Asp61 protonated	8 ps
5		LS	10 ps
6		LS, W3 deprotonated, Asp61 protonated	8 ps
7	S_3Y_z	HS	9 ps
8		LS	10 ps
		Total:	75 ps

Table S4. List of performed atomistic MD simulations. AspH/Asp^- refer to protonated/deprotonated Asp61.

Nr.	State	Temperature	Length
1	S_2Y_z	300 K	200 ns
2			
3		320 K	
4	$S_2Y_z^\bullet$	300 K	200 ns
5			
6		320 K	
7	S_3Y_z (AspH)	300 K	200 ns
8			
9		320 K	
10	S_3Y_z (Asp^-)	310 K	200 ns
11		320 K	
12	$S_3Y_z^\bullet$	310 K	200 ns
13		320 K	
14	S_4Y_z	310 K	200 ns
15		320 K	
		Total:	**3000 ns**

Table S5. Frequency (in cm^{-1}) of the transition states (TS)/ saddle points obtained from DFT reaction pathway optimization. The reported frequencies were computed at the B3LYP-D3/def2-SVP/def2-TZVP(Mn,Ca)/ε=4 level of theory.

	S_2Y_z		$S_2Y_z^{\bullet} \rightarrow S_3Y_z$		S_3Y_z	$S_3Y_z^{\bullet}$
	HS/closed	**LS/open**	**HS/closed**	**LS/open**	**LS/open**	**LS/open**
TS / Saddle point 1 [cm^{-1}]	-644.1	-70.3	-646.6	-124.5	-331.2	-484.9
TS / Saddle point 2 [cm^{-1}]	-1108.5	-534.5	-986.5	-681.3	-588.6	-484.3

Table S6. Comparison of experimental and computational distances of the Mn_4O_5Ca cluster in different states. The experimental errors of the refined oxygen positions are expected to be in the range of around 0.2 Å (based on the resolution of 1.9-2.4 Å). Unresolved distances marked with *n/a*. Models of the S_2Y_z state marked with an asterisk.

S_3Y_z	Mn1-Ox/W3	Mn4-O5	Ox/W3-O5	O-Mn1-Ox (deg)	Mn4-W1	Mn4-W2	Ca-O5
Current work	1.8	1.8	2.4	100	2.0	1.9	3.1
3WU2*	n/a	2.4	n/a	n/a	2.3	2.1	2.4
6JLL (2F, dataset1)	1.7	2.2	1.9	111	2.2	2.1	2.6
6JLO (2F, dataset2)	1.7	2.2	1.9	89	2.2	2.1	2.6
5WS6 (preflash)	2.3	2.3	1.5	103	2.2	2.1	2.5
7RF4 (2F, 50 µs)*	n/a	2.0	n/a	n/a	2.1	2.2	2.6
7RF5 (2F, 150 µs)	1.8	2.2	2.1	111	2.1	2.2	2.6
7RF6 (2F, 200 µs)	1.8	2.2	2.1	109	2.1	2.1	2.6
7RF7 (2F, 400 µs)	1.8	2.2	2.1	111	2.1	2.1	2.7
7RF8 (2F, 200 ms)	1.8	2.2	2.0	111	2.0	2.1	2.6
6w1q (2F, 50 µs)*	n/a	2.0	n/a	n/a	2.1	2.1	2.6
6w1r (2F, 150 µs)	1.8	2.3	1.9	101	2.2	2.1	2.6
6w1t (2F, 250 µs)	1.7	2.3	1.9	101	2.1	2.3	2.6
6w1u (2F, 400 µs)	1.6	2.2	2.1	102	2.1	2.2	2.5
6w1v (2F, 200 ms)	1.7	2.1	2.1	112	2.1	2.1	2.6
Siegbahn 2013	1.8	1.8	2.5	100	2.0	1.8	2.6
Batista 2016	1.8	1.8	2.4	101	1.9	2.2	3.0
Kaila 2016	1.8	1.9	2.5	97	2.0	1.8	2.4
Yamaguchi 2016	1.8	1.8	2.4	99	2.0	1.8	2.7
Pantazis 2021	1.8	1.8	2.5	97	2.0	1.8	2.7

Structures/models: 3WU2,[23] 5WS6,[24] 6JLL and 6JLO,[25] 6W1Q-6W1V,[26] 7RF4-7RF8,[27] Siegbahn 2013,[28] Batista 2016,[29] Kaila 2016,[4] Yamaguchi 2016,[30] Pantazis 2021.[31]

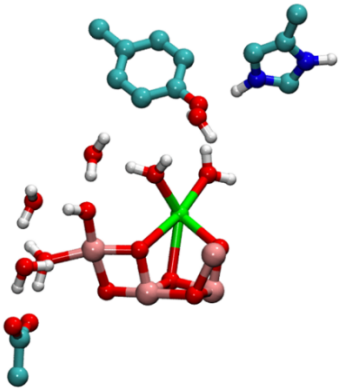

Movie S1. Proton transfer between W3 and Asp61 in the LS/open cubane form of the $S_2Y_z^{\bullet}$ state obtained by reaction pathway optimization. The energetics along this pathway are shown in main text Figure 2A.

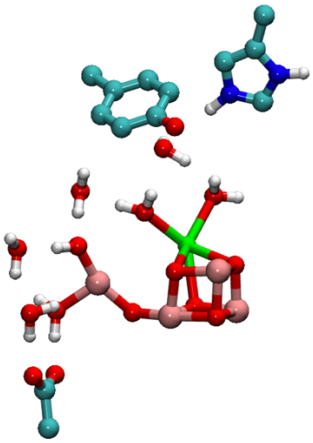

Movie S2. Proton transfer between W3 and Asp61 in the HS/closed cubane form of the $S_2Y_z^{\bullet}$ state obtained by reaction pathway optimization. The energetics along this pathway are shown in main text Figure 2A.

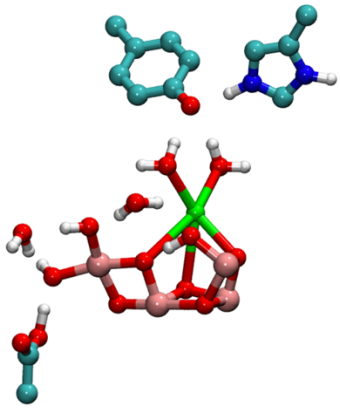

Movie S3. Proton transfer between Mn1-bound W3(OH^-) and Asp61 in the LS/open cubane form of the $S_3Y_z^{\bullet}$ state obtained by reaction pathway optimization. The energetics along this pathway are shown in main text Figure 3A.

SI References

1. Bovi, D.; Narzi, D.; Guidoni, L., The S_2 State of the Oxygen-Evolving Complex of Photosystem II Explored by QM/MM Dynamics: Spin Surfaces and Metastable States Suggest a Reaction Path Towards the S_3 State. *Angew. Chem. Int. Ed. Engl.* **2013,** *52*, 11744-11749.
2. Boussac, A.; Girerd, J.-J.; Rutherford, A. W., Conversion of the Spin State of the Manganese Complex in Photosystem II Induced by Near-Infrared Light. *Biochemistry* **1996,** *35*, 6984-6989.
3. Boussac, A.; Ugur, I.; Marion, A.; Sugiura, M.; Kaila, V. R. I.; Rutherford, A. W., The low spin - high spin equilibrium in the S_2-state of the water oxidizing enzyme. *Biochim. Biophys. Acta Bioenerg.* **2018,** *1859*, 342-356.
4. Ugur, I.; Rutherford, A. W.; Kaila, V. R. I., Redox-coupled substrate water reorganization in the active site of Photosystem II—The role of calcium in substrate water delivery. *Biochim. Biophys. Acta Bioenerg.* **2016,** *1857*, 740-748.
5. Retegan, M.; Krewald, V.; Mamedov, F.; Neese, F.; Lubitz, W.; Cox, N.; Pantazis, D. A., A five-coordinate Mn(iv) intermediate in biological water oxidation: spectroscopic signature and a pivot mechanism for water binding. *Chem. Sci.* **2016,** *7*, 72-84.
6. Shoji, M.; Isobe, H.; Yamaguchi, K., QM/MM study of the S_2 to S_3 transition reaction in the oxygen-evolving complex of photosystem II. *Chem. Phys. Lett.* **2015,** *636*, 172-179.
7. Isobe, H.; Shoji, M.; Yamanaka, S.; Umena, Y.; Kawakami, K.; Kamiya, N.; Shen, J.-R.; Yamaguchi, K., Theoretical illumination of water-inserted structures of the CaMn4O5 cluster in the S2 and S3 states of oxygen-evolving complex of photosystem II: full geometry optimizations by B3LYP hybrid density functional. *Dalton Trans.* **2012,** *41*, 13727.
8. Cser, K.; Diner, B.A., Nixon, P.J., Vass, I. The role of D1-Ala344 in charge stabilization and recombination in Photosystem II. *Photochem Photobiol Sci.* **2005**, *4*, 1049-1054.
9. Retegan, M.; Cox, N.; Lubitz, W.; Neese, F.; Pantazis, D. A., The first tyrosyl radical intermediate formed in the S_2–S_3 transition of photosystem II. *Phys. Chem. Chem. Phys.* **2014,** *16*, 11901.
10. Capone, M.; Bovi, D.; Narzi, D.; Guidoni, L., Reorganization of Substrate Waters between the Closed and Open Cubane Conformers during the S2 to S3 Transition in the Oxygen Evolving Complex. *Biochemistry* **2015,** *54*, 6439-6442.
11. Capone, M.; Narzi, D.; Bovi, D.; Guidoni, L., Mechanism of Water Delivery to the Active Site of Photosystem II along the S2 to S3 Transition. *J. Phys. Chem. Lett.* **2016,** *7*, 592-596.
12. Wang, J.; Askerka, M.; Brudvig, G. W.; Batista, V. S., Crystallographic Data Support the Carousel Mechanism of Water Supply to the Oxygen-Evolving Complex of Photosystem II. *ACS Energy Lett.* **2017,** *2*, 2299-2306.
13. Lee, C.; Yang, W.; Parr, R. G., Development of the Colle-Salvetti correlation-energy formula into a functional of the electron density. *Phys. Rev. B* **1988,** *37*, 785-789.
14. Schäfer, A.; Horn, H.; Ahlrichs, R., Fully optimized contracted Gaussian basis sets for atoms Li to Kr. *J. Chem. Phys.* **1992,** *97*, 2571-2577.
15. Becke, A. D., Density-functional thermochemistry. III. The role of exact exchange. *J. Chem. Phys.* **1993,** *98*, 5648-5652.
16. Grimme, S.; Antony, J.; Ehrlich, S.; Krieg, H., A consistent and accurate ab initio parametrization of density functional dispersion correction (DFT-D) for the 94 elements H-Pu. *J. Chem. Phys.* **2010,** *132*, 154104.
17. Reiher, M.; Salomon, O.; Artur Hess, B., Reparameterization of hybrid functionals based on energy differences of states of different multiplicity. *Theo. Chem. Acc.: Theory, Comp. Model. (Theoretica Chimica Acta)* **2001,** *107*, 48-55.
18. Staroverov, V. N.; Scuseria, G. E.; Tao, J.; Perdew, J. P., Comparative assessment of a new nonempirical density functional: Molecules and hydrogen-bonded complexes. *J. Chem. Phys.* **2003,** *119*, 12129-12137.
19. Becke, A. D., A new mixing of Hartree–Fock and local density-functional theories. *J. Chem. Phys.* **1993,** *98*, 1372-1377.
20. Yanai, T.; Tew, D. P.; Handy, N. C., A new hybrid exchange–correlation functional using the Coulomb-attenuating method (CAM-B3LYP). *Chem. Phys. Lett.* **2004,** *393*, 51-57.
21. Shao, Y.; Mei, Y.; Sundholm, D.; Kaila, V. R. I., Benchmarking the Performance of Time-Dependent Density Functional Theory Methods on Biochromophores. *J. Chem. Theo. Comput.* **2020,** *16*, 587-600.
22. Perdew, J. P.; Ernzerhof, M.; Burke, K., Rationale for mixing exact exchange with density functional approximations. *J. Chem. Phys.* **1996,** *105*, 9982-9985.
23. Umena, Y.; Kawakami, K.; Shen, J.-R.; Kamiya, N., Crystal structure of oxygen-evolving photosystem II at a resolution of 1.9 Å. *Nature* **2011,** *473*, 55-60.
24. Suga, M.; Akita, F.; Sugahara, M.; Kubo, M.; Nakajima, Y.; Nakane, T.; Yamashita, K.; Umena, Y.; Nakabayashi, M.; Yamane, T.; Nakano, T.; Suzuki, M.; Masuda, T.; Inoue, S.; Kimura, T.; Nomura, T.; Yonekura, S.; Yu, L.-J.; Sakamoto, T.; Motomura, T.; Chen, J.-H.; Kato, Y.; Noguchi, T.; Tono, K.; Joti, Y.; Kameshima, T.; Hatsui, T.; Nango, E.; Tanaka, R.; Naitow, H.; Matsuura, Y.; Yamashita, A.; Yamamoto, M.; Nureki, O.; Yabashi,

M.; Ishikawa, T.; Iwata, S.; Shen, J.-R., Light-induced structural changes and the site of O=O bond formation in PSII caught by XFEL. *Nature* **2017,** *543*, 131-135.
25. Suga, M.; Akita, F.; Yamashita, K.; Nakajima, Y.; Ueno, G.; Li, H.; Yamane, T.; Hirata, K.; Umena, Y.; Yonekura, S.; Yu, L.-J.; Murakami, H.; Nomura, T.; Kimura, T.; Kubo, M.; Baba, S.; Kumasaka, T.; Tono, K.; Yabashi, M.; Isobe, H.; Yamaguchi, K.; Yamamoto, M.; Ago, H.; Shen, J.-R., An oxyl/oxo mechanism for oxygen-oxygen coupling in PSII revealed by an x-ray free-electron laser. *Science* **2019,** *366*, 334-338.
26. Ibrahim, M.; Fransson, T.; Chatterjee, R.; Cheah, M. H.; Hussein, R.; Lassalle, L.; Sutherlin, K. D.; Young, I. D.; Fuller, F. D.; Gul, S.; Kim, I.-S.; Simon, P. S.; De Lichtenberg, C.; Chernev, P.; Bogacz, I.; Pham, C. C.; Orville, A. M.; Saichek, N.; Northen, T.; Batyuk, A.; Carbajo, S.; Alonso-Mori, R.; Tono, K.; Owada, S.; Bhowmick, A.; Bolotovsky, R.; Mendez, D.; Moriarty, N. W.; Holton, J. M.; Dobbek, H.; Brewster, A. S.; Adams, P. D.; Sauter, N. K.; Bergmann, U.; Zouni, A.; Messinger, J.; Kern, J.; Yachandra, V. K.; Yano, J., Untangling the sequence of events during the $S_2 \rightarrow S_3$ transition in photosystem II and implications for the water oxidation mechanism. *Proc. Nat. Acad. Sci. U. S. A.* **2020,** *117*, 12624-12635.
27. Hussein, R.; Ibrahim, M.; Bhowmick, A.; Simon, P. S.; Chatterjee, R.; Lassalle, L.; Doyle, M.; Bogacz, I.; Kim, I.-S.; Cheah, M. H.; Gul, S.; De Lichtenberg, C.; Chernev, P.; Pham, C. C.; Young, I. D.; Carbajo, S.; Fuller, F. D.; Alonso-Mori, R.; Batyuk, A.; Sutherlin, K. D.; Brewster, A. S.; Bolotovsky, R.; Mendez, D.; Holton, J. M.; Moriarty, N. W.; Adams, P. D.; Bergmann, U.; Sauter, N. K.; Dobbek, H.; Messinger, J.; Zouni, A.; Kern, J.; Yachandra, V. K.; Yano, J., Structural dynamics in the water and proton channels of photosystem II during the S_2 to S_3 transition. *Nat. Commun.* **2021,** *12*.
28. Siegbahn, P. E. M., Water oxidation mechanism in photosystem II, including oxidations, proton release pathways, O—O bond formation and O_2 release. *Biochim. Biophys. Acta Bioenerg.* **2013,** *1827*, 1003-1019.
29. Askerka, M.; Wang, J.; Vinyard, D. J.; Brudvig, G. W.; Batista, V. S., S_3 State of the O2-Evolving Complex of Photosystem II: Insights from QM/MM, EXAFS, and Femtosecond X-ray Diffraction. *Biochemistry* **2016,** *55*, 981-984.
30. Isobe, H.; Shoji, M.; Shen, J.-R.; Yamaguchi, K., Chemical Equilibrium Models for the S3 State of the Oxygen-Evolving Complex of Photosystem II. *Inorg. Chem.* **2016,** *55*, 502-511.
31. Drosou, M.; Pantazis, D. A., Redox Isomerism in the S_3 State of the Oxygen-Evolving Complex Resolved by Coupled Cluster Theory. *Chem.- Eur. J.* **2021,** *27*, 12815-12825.